Bias Dependence of Non-Fourier Heat Spreading in GaN HEMTs

Yang Shen, Xue-Song Chen, Yu-Chao Yuchao Hua, Han-Ling Li, Lan Wei, Bing-Yang Cao

To cite this version:

Yang Shen, Xue-Song Chen, Yu-Chao Yuchao Hua, Han-Ling Li, Lan Wei, et al.. Bias Dependence of Non-Fourier Heat Spreading in GaN HEMTs. IEEE Transactions on Electron Devices, 2023, 70 (2), pp.409-417. 10.1109/TED.2022.3227894 . hal-04047529

HAL Id: hal-04047529
https://hal.science/hal-04047529v1

Bias Dependence of Non-Fourier Heat Spreading in GaN HEMTs

Yang Shen, Xue-Song Chen, Yu-Chao Hua, Han-Ling Li, Lan Wei, Bing-Yang Cao

***Abstract*—In this paper, self-heating in gallium nitride (GaN) high-electron-mobility transistors (HEMTs) is studied by combining the technology computer-aided design (TCAD) and phonon Monte Carlo (MC) simulations. The simulation results indicate that the bias-dependent heat generation in the channel can have a remarkable impact on the thermal spreading process and the phonon ballistic effects simultaneously. Based on the two-heat-source model, we propose a two-thermal-conductivity model to predict the device junction temperature with the consideration of bias-dependent phonon transport in the HEMT. The proposed model is easy to be coupled with the finite element method (FEM)-based thermal analysis without the need for time-consuming multiscale electrothermal simulations.**

***Index Terms*—Electrothermal simulation, gallium nitride (GaN) high-electron-mobility transistor (HEMT), ballistic transport, phonon Monte Carlo (MC) simulation.**

I. INTRODUCTION

Gallium nitride (GaN)-based high electron mobility transistors (HEMTs) are attractive for high-power amplifiers and high-frequency switching applications [1]. Due to the wide bandgap of GaN and the two-dimensional electron gas (2DEG) formed at the AlGaN/GaN heterojunction, GaN HEMTs can sustain a high voltage and exhibit an excellent electron mobility [2]. However, owing to the high power density, significant self-heating in GaN HEMTs can degrade the device performance and shorten the device lifetime [3]–[5]. To accurately predict the junction temperature thereby develop effective thermal management strategies, it's important to clearly understand the heat generation and transport process in GaN HEMTs.

The heat in the HEMT is primarily generated on the top of the GaN buffer layer with a width of about a few hundred nanometers and dissipated through the GaN layer to the substrate [6], [7]. The thickness of the GaN layer usually ranges from $1\,\mu\mathrm{m}$ to $3\,\mu\mathrm{m}$, and the thickness of the substrate can be larger than $100\,\mu\mathrm{m}$. Compared with the total device length and thickness, the heat source area of the HEMT is very small [8]. When heat spreads from a small area to a much larger region, there is a significant thermal spreading resistance which can dominate the thermal transport process within the HEMT [9]. In addition, the main heat carriers in GaN are phonons whose mean free paths (MFPs) are generally larger than $100\,\mathrm{nm}$ [10], [11], which are comparable with the thickness of the GaN layer and the width of the heat generation region. The frequent boundary and interface scattering can lead to a reduced thermal conductivity of the GaN thin films [12], and the quasi-ballistic transport when the heat source size is comparable with the phonon MFP can further increase the hotspot temperature [13]–[15].

Based on Fourier's law of heat conduction, the thermal spreading process has been studied extensively, including the cases with eccentric heat sources [16], interfacial thermal resistance [17], anisotropic and temperature-dependent thermal conductivities [18], [19], *etc*. Hua *et al.* investigated the thermal spreading resistance in a ballistic-diffusive regime and demonstrated that the phonon ballistic effects could result in a dramatic increase in the thermal resistance compared with Fourier's law-based predictions [20]. In addition, the results indicate that the strength of the phonon ballistic effects can be significantly related to the geometric size of the system and the width of the heating area. Recently, the effect of phonon dispersion and the heating scheme on the thermal resistance of devices have also been studied [21], [22].

However, most of these studies assume that the heat source has the same length as the gate which is modeled as either a surface heat flux or a uniform volumetric heat source on the top of the GaN layer. Whereas being the result of Joule heating, the heat generation in the HEMT is highly bias-dependent [23], [24]. At different biases, the heat source distributions in the channel can be quite different, which can have a marked impact on the thermal spreading process and the strength of the phonon ballistic effects. This necessitates the examination of the influence of the bias-dependent heat generation on the thermal spreading process and phonon ballistic effects simultaneously. Though there has been some work on multiscale electrothermal simulations [25]–[29] indicating that the phonon ballistic effects can increase the device junction temperature compared with Fourier's law-based predictions, the quantitative analysis of bias-dependent phonon ballistic transport in GaN HEMTs has not been carried out.

This work was supported by the National Natural Science Foundation of China (Nos. 51825601,U20A20301). (Corresponding author: Bing-Yang Cao.)

Yang Shen, Han-Ling Li, Bing-Yang Cao are with the Key Laboratory of Thermal Science and Power Engineering of Education of Ministry, Department of Engineering Mechanics, Tsinghua University, Beijing 100084, China (e-mail: sy980829@163.com; lihanling1994@163.com; caoby@tsinghua.edu.cn).

Yu-Chao Hua is with the LTEN laboratory, Polytech Nantes, University of Nantes, UMR6607, F-44000, Nantes, France (e-mail: huayuchao19@163.com).

Xue-Song Chen and Lan Wei are with the Department of Electrical and Computer Engineering, University of Waterloo, Waterloo, ON N2L 3G1, Canada (e-mail: xschen08@gmail.com; lan.wei@uwaterloo.ca).

In this work, we reexamine self-heating in GaN HEMTs by combining the technology computer-aided design (TCAD) and phonon Monte Carlo (MC) simulations. It is found that the bias-dependent heat generation in the channel can have a remarkable impact on the thermal spreading process and the phonon ballistic effects simultaneously. Based on the two-heat-source model, we propose a two-thermal-conductivity model that can easily reflect the influence of the bias-dependent non-Fourier heat spreading process in GaN HEMTs, without resorting to multiscale electrothermal simulations.

II. SIMULATION METHODOLOGY

A. TCAD Simulations

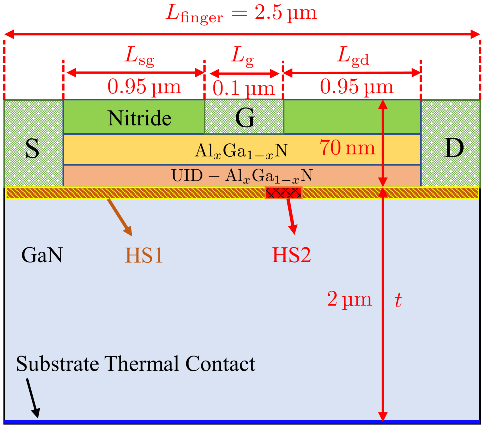

Fig. 1. Schematic of the GaN HEMT for TCAD simulations. S, G, D refer to the source, gate, and drain, respectively.

The GaN HEMT for TCAD simulations is shown in Fig. 1, which follows the structure of the device presented in Ref. [30]. From top to bottom, the layers are a $50\,\text{nm}$ silicon nitride passivation layer, an $18\,\text{nm}$ $\text{Al}_{0.25}\text{Ga}_{0.75}\text{N}$ layer with donor concentration $N_{\text{D}} = 2 \times 10^{18}\,\text{cm}^{-3}$, a $2\,\text{nm}$ unintentionally doped (UID) $\text{Al}_{0.25}\text{Ga}_{0.75}\text{N}$ spacer layer with donor concentration $N_{\text{D}} = 1 \times 10^{15}\,\text{cm}^{-3}$, a $2\,\mu\text{m}$ GaN buffer layer and a $10\,\text{nm}$ SiC substrate layer. The gate length is $L_{\text{g}} = 0.1\,\mu\text{m}$, the source and drain access regions have the same length of $L_{\text{sg}} = L_{\text{gd}} = 0.95\,\mu\text{m}$. The total length of the activated region is $L_{\text{finger}} = 2.5\,\mu\text{m}$.

Electrothermal TCAD simulations are conducted to predict the heat generation profiles at different biases, which are used to drive the phonon MC simulations. Since the focus of this work is the influence of bias-dependent heat generation on the thermal transport process, detailed electron-phonon interactions are not considered in the current study [31]. The drift-diffusion model (DDM) is used for electron transport [32], which assumes that electrons are in thermal equilibrium with the lattice. To consider the non-equilibrium energy transfer between electrons and phonons, electron MC simulations can be carried out to give the detailed phonon generation spectrum [33]. Figure 2 shows the simulated output characteristics of the HEMT, which shows a good agreement with the experimental results.

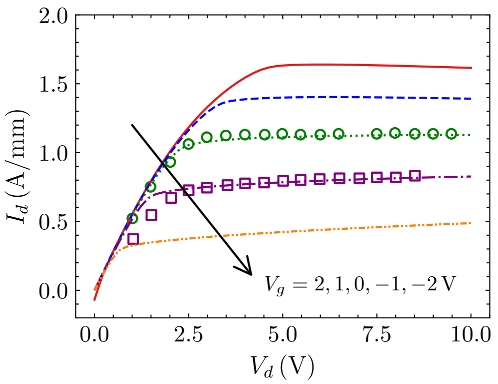

Fig. 2. Output characteristics of the HEMT from $-2\,\text{V}$ to $2\,\text{V}$ with an interval of $1\,\text{V}$ extracted from TCAD simulations (lines) and experimental results (symbols) [30].

B. Phonon Monte Carlo Simulations

The phonon tracing MC simulation is an effective approach to simulate the ballistic-diffusive heat conduction, which can deal with the transport problems involving complex geometries, multiple interfaces, and arbitrary heat source distributions [34]. The detailed principles and procedures can be found in Ref. [35]–[37]. Figure 3 shows the schematic of the GaN-on-SiC device for the MC simulations, which is a typical structure for a period of multi-finger GaN HEMT devices with a pinch distance $w = 30\,\mu\text{m}$. The heat source only exists in the TCAD simulated region which is in the center of the device between the source and drain. Since the thin AlGaN layer has a very low thermal conductivity and the heat generation mainly exists in the GaN layer, the structures above the AlGaN/GaN interface are all neglected in the MC simulation [38]. The boundaries in the lateral direction are set as periodic, and the top boundary is adiabatic. Given that the heat conduction in the substrate is almost a one-dimensional process, the simulation thickness for the substrate in this work is only set as $30\,\mu\text{m}$, and the bottom is set as isothermal. For real device simulations, the bottom boundary condition can be easily changed to the non-uniform temperature distributions calculated using Fourier's law-based simulations [25]–[28].

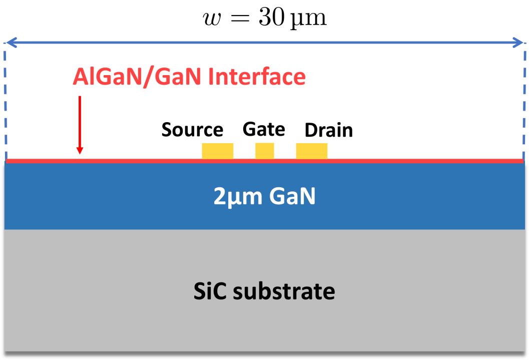

Fig. 3. Schematic of the GaN-on-SiC device for the phonon MC simulations, the TCAD simulation region is between the source and drain. The geometries are not drawn to scale.

The phonon dispersion and relaxation time are needed to carry out the MC simulations. In this work, an isotropic sine-shaped phonon dispersion (Born-von Karman dispersion) is used for both GaN and SiC. In the dispersion model, the relation between the angular frequency ω and wave vector k can be depicted as $\omega(k) = \omega_{\mathrm{m}} \sin(\pi k/2k_{\mathrm{m}})$, where $k_{\mathrm{m}} = (6\pi^2 n)^{1/3}$ with n as the volumetric density of primitive cells. The previous research has verified that this dispersion model can well reflect the phonon MFP spectrum of various materials [10]. The scattering mechanisms considered in this work include impurity scattering (I) and Umklapp scattering (U), and only point defects are included in the impurity scattering since the previous work has indicated that these scattering mechanisms are the most essential ones in GaN [26], [39]. The relaxation time can be expressed as $\tau_{\mathrm{I}}^{-1} = A\omega^4$ and $\tau_{\mathrm{U}}^{-1} = B\omega^2 T \exp(-C/T)$, where A, B, and C are the fitting constants. The total relaxation time can be calculated using Matthiessen's rule $\tau^{-1} = \tau_{\mathrm{I}}^{-1} + \tau_{\mathrm{U}}^{-1}$ [40]. This work adopts the fitted parameters in Ref. [26], as shown in Tab. I. The model calculated bulk thermal conductivities of GaN and SiC are $220\,\mathrm{W/m\,K}$ and $350\,\mathrm{W/m\,K}$, respectively, which is in agreement with the experimental values [41]. To better depict the phonon scattering process, more scattering mechanisms such as dislocation scattering [42], grain boundary scattering [43], and normal phonon scattering [44] *etc.* can be included based on first-principle calculations in the future work.

TABLE I
PHONON DISPERSION AND SCATTERING PARAMETERS.

Parameter (Unit)	GaN	SiC
$k_0\,(1\times10^{9}\,\mathrm{m}^{-1})$	10.94	8.94
$\omega_m\,(1\times10^{13}\,\mathrm{rad/s})$	3.50	7.12
a_D (Å)	2.87	3.51
$A\,(1\times10^{-45}\,\mathrm{s}^3)$	5.26	1.00
$B\,(1\times10^{-19}\,\mathrm{s/K})$	1.10	0.596
C (K)	200	235.0

To describe phonon transport in the GaN/SiC interface, the diffuse mismatch model (DMM) is used to calculate the interface phonon transmissivities [45]. In DMM, phonons are diffusively transmitted or reflected by an interface, and the phonon transmissivity with frequency ω from material 1 to 2 can be expressed as

$$T_{12}(\omega) = \frac{\sum_p v_{2,g,p}(\omega) D_{2,p}(\omega)}{\sum_p v_{1,g,p}(\omega) D_{1,p}(\omega) + \sum_p v_{2,g,p}(\omega) D_{2,p}(\omega)}, \tag{1}$$

where p is the phonon branch, $v_g(\omega)$ is the phonon group velocity, and $D(\omega)$ is the density of states. The thermal boundary resistance (TBR) of the GaN/SiC interface calculated using the MC simulations is $16\,\mathrm{m^2\,K/GW}$, which is in the same range as the experimental results ($4\,\mathrm{m^2\,K/GW}$–$20\,\mathrm{m^2\,K/GW}$) [46]–[49]. DMM only includes harmonic interfacial phonon-phonon scatterings and ignores the contribution of anharmonic interactions [50]. The full-band phonon dispersion and interfacial transmissivities are expected to be incorporated in the phonon MC simulations to simulate the near-junction thermal transport process more accurately [51]–[53].

III. RESULTS AND DISCUSSION

A. Bias-Dependent Heat Generation

Figure 4 shows the heat generation profiles in the channel at two biases with an identical power dissipation $P_{\mathrm{diss}} = 5\,\mathrm{W/mm}$ extracted from TCAD simulations. The heat generation mainly exists within a $2\,\mathrm{nm}$ region below the AlGaN/GaN interface and is highly bias-dependent. At $V_{\mathrm{g}} = 2\,\mathrm{V}$, the heat spans relatively uniformly in the whole channel. Whereas for the condition at $V_{\mathrm{g}} = -1\,\mathrm{V}$, the heat is concentrated at the drain-side gate edge with a much larger heat density.

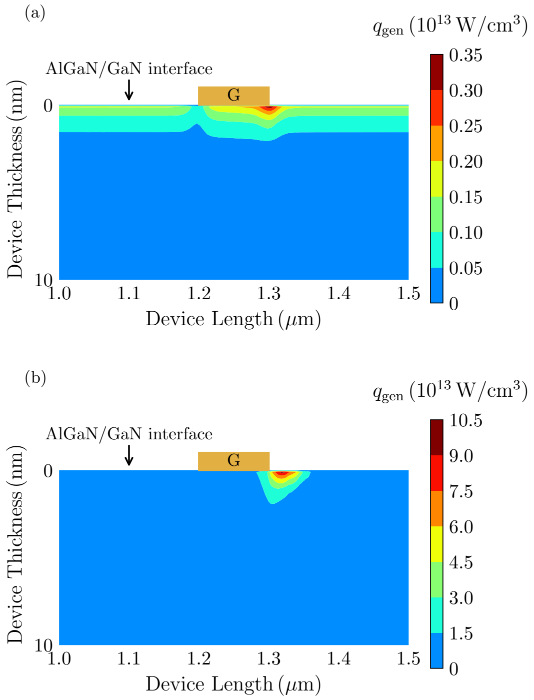

Fig. 4. Heat generation in the channel extracted from TCAD simulations at two biases (a) $\boldsymbol{V}_{\mathrm{g}} = 2\,\mathrm{V}, \boldsymbol{V}_{\mathrm{d}} = 3.8\,\mathrm{V}$, and (b) $\boldsymbol{V}_{\mathrm{g}} = -1\,\mathrm{V}, \boldsymbol{V}_{\mathrm{d}} = 6.7\,\mathrm{V}$ with an identical power dissipation $\boldsymbol{P}_{\mathrm{diss}} = 5\,\mathrm{W/mm}$.

To represent the bias-dependent heat generation caused by the non-uniform electric field in the channel, Chen *et al.* proposed a two-heat-source model which divided the total heat dissipation into two parts [32], as shown in Fig. 1. Heat Source 1 (HS1) spanning the whole finger length (L_{finger}) represents the relatively low and uniform heat generation in the channel. Heat Source 2 (HS2) centered at the drain-side gate edge represents the concentrated heat generation under the high electric field. The length of HS1 (L_{HS1}) is the same as the finger length, and the length of HS2 (L_{HS2}) is set as $0.16\,\mu\mathrm{m}$ to approximate the length of the high-field region. L_{HS2} is independent of the bias and device geometry since the width of the high-field region nearly does not change with these parameters [23], [24], [32]. When the device is in the linear regime, *i.e.* V_{d} is less than the drain saturation voltage V_{dsat}, all the heat is dissipated in HS1. As the channel is pinched-off and the device works in the saturation regime, *i.e.* $V_{\mathrm{d}} > V_{\mathrm{dsat}}$, the heat dissipated in HS1 stays the maximum and the excessive heat is only dissipated in HS2. The model can be expressed as,

$$\begin{cases} P_1 = I_\mathrm{d} V_\mathrm{d}, P_2 = 0, & V_\mathrm{d} \le V_\mathrm{dsat} \\ P_1 = I_\mathrm{d} V_\mathrm{dsat}, P_2 = I_\mathrm{d}\left(V_\mathrm{d} - V_\mathrm{dsat}\right), & V_\mathrm{d} > V_\mathrm{dsat} \end{cases} \qquad (2)$$

where P_1 and P_2 are the power dissipations in HS1 and HS2, respectively. Figure 5 shows the power dissipated in the two heat sources predicted by equation (2) and extracted from TCAD simulations at $P_\mathrm{diss} = 5\,\mathrm{W/mm}$. A good agreement is achieved at different biases. Also, it can be found that at the same power dissipation, more heat is dissipated in HS2 for the bias with a lower V_g since the device has to work deeper to maintain the same P_diss.

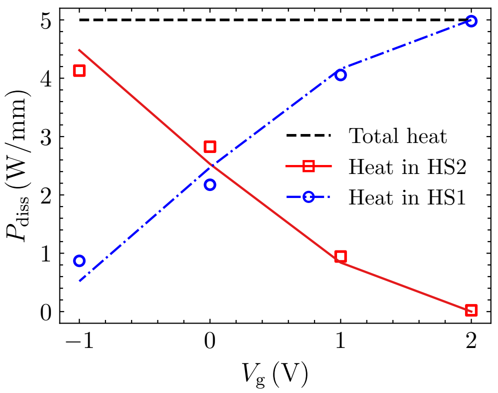

Fig. 5. Heat dissipation in HS1 and HS2 with an identical power dissipation $P_\mathrm{diss} = 5\,\mathrm{W/mm}$ predicted by the two-heat-source model (lines) and extracted from TCAD simulations (symbols). The four bias points are $(V_\mathrm{g}, V_\mathrm{d}) = (-1\,\mathrm{V}, 6.7\,\mathrm{V})$, $(0\,\mathrm{V}, 5\,\mathrm{V})$, $(1\,\mathrm{V}, 4.1\,\mathrm{V})$, and $(2\,\mathrm{V}, 3.8\,\mathrm{V})$.

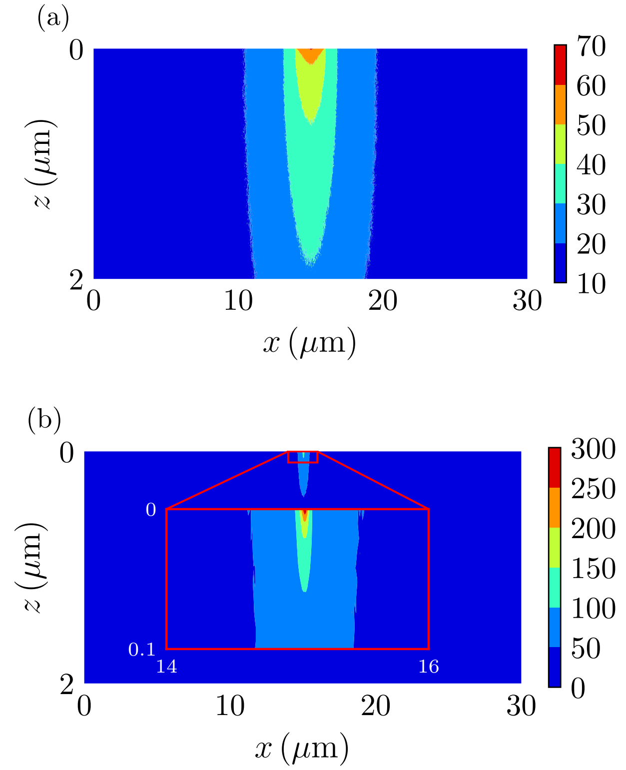

Fig. 6. Temperature rise distributions in the GaN layer at different biases (a) $V_\mathrm{g} = 2\,\mathrm{V}, V_\mathrm{d} = 3.8\,\mathrm{V}$ and (b) $V_\mathrm{g} = -1\,\mathrm{V}, V_\mathrm{d} = 6.7\,\mathrm{V}$ predicted by the MC simulations with an identical power dissipation $P_\mathrm{diss} = 5\,\mathrm{W/mm}$.

B. Temperature Distribution in the HEMT

Figure 6 shows the temperature rise distributions relative to the heat sink in the GaN layer predicted by the MC simulations at two biases with an identical power dissipation $P_\mathrm{diss} = 5\,\mathrm{W/mm}$. At $V_g = 2\,\mathrm{V}$, the maximum temperature rise is around $70\,\mathrm{K}$. Whereas at $V_g = -1\,\mathrm{V}$, the maximum temperature rise can reach about $300\,\mathrm{K}$. The results can be explained by Fig.5, at $V_g = 2\,\mathrm{V}$ the heat is almost dissipated in HS1. Whereas at $V_g = -1\,\mathrm{V}$, most heat is dissipated in HS2 with a much smaller size. The decrease of the heat source size can result in a much larger thermal spreading resistance and the ballistic effect with the heat source size comparable with MFP. Also, it is revealed by the comparison that the ballistic effect can significantly change the temperature profiles. As the size of the heat source decreases, the lack of internal phonon scatterings can cause the temperatures to decay more rapidly away from the hot area. At $V_\mathrm{g} = 2\,\mathrm{V}$, the temperature change in the whole GaN layer is less than $60\,\mathrm{K}$, whereas at $V_\mathrm{g} = -1\,\mathrm{V}$, the temperature drops by nearly $200\,\mathrm{K}$ in a $50\,\mathrm{nm}$ range along thickness.

Figure 7 compares the temperature rise distributions at the drain-side gate edge along thickness predicted by the MC simulations at the two biases. The results predicted by the finite element method (FEM) with the bulk thermal conductivities are also given for comparison. Compared with the FEM results, the temperatures predicted by the MC simulations are much higher in the hotspot region due to the strong phonon ballistic effects. As the distance away from the hotspot increases, the MC simulation temperatures gradually become consistent with the FEM results, since the phonon scattering enhances and the heat starts to transport in a diffusive way. In addition, it more clearly shows that the size of the heat source can have a remarkable influence on the hotspot temperature distributions. At the bias with a lower V_g, the heat source size-induced ballistic effect can significantly increase the maximum temperature and decays rapidly away from the hotspot.

The channel temperature profiles predicted by the MC simulations and FEM at the two biases are also plotted in Fig. 8. It can be found that due to the different heat generation profiles, the temperature distributions exhibit a very distinct behavior. At $V_\mathrm{g} = 2\,\mathrm{V}$, the heat spans relatively uniformly in HS1 with a low heat density. In this case, the temperature distributions in the heat source region are smooth and the difference between the MC simulations and FEM is not too significant due to the relatively weak phonon ballistic effect. Whereas at $V_\mathrm{g} = -1\,\mathrm{V}$, the heat generation is highly concentrated in HS2 with a small size and the strong phonon ballistic effect leads to a dramatic increase in the hotspot temperature. The same phenomenon can be also observed from the experimental results [28].

C. Thermal Resistance of the GaN Layer

As shown in Fig. 7, since the heat transports nearly diffusively away from the heat source, this work mainly focuses

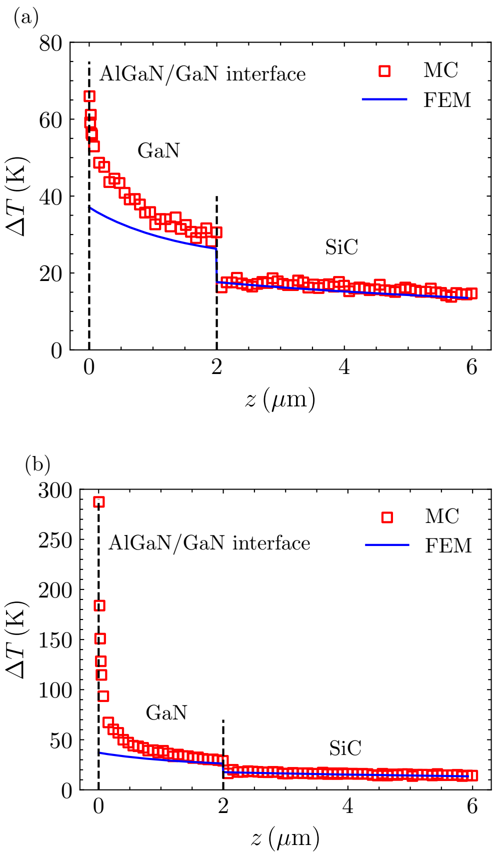

Fig. 7. Comparison of the temperature rise distributions through the depth of the HEMT at drain-side gate edge (a) $\boldsymbol{V}_{\mathrm{g}} = 2\,\mathrm{V}, \boldsymbol{V}_{\mathrm{d}} = 3.8\,\mathrm{V}$ and (b) $\boldsymbol{V}_{\mathrm{g}} = -1\,\mathrm{V}, \boldsymbol{V}_{\mathrm{d}} = 6.7\,\mathrm{V}$ with an identical power dissipation $\boldsymbol{P}_{\mathrm{diss}} = 5\,\mathrm{W/mm}$ computed by the MC simulations and FEM.

on analyzing the bias dependence of the thermal resistance of the GaN layer. Figure 9 shows the temperature rise in the GaN layer ΔT_{GaN} as a function of the power dissipation P_{diss} extracted from the MC simulations and FEM at the two biases. To reduce the statistical uncertainty and moderate the influence of the non-local electron transport in a peaked electric region [26], [54], the maximum temperature defined in this work is the average temperature of HS2. As shown in Fig. 9, for both biases, the curve of ΔT_{GaN} against P_{diss} can be divided into two parts. When the device works in the linear regime, ΔT_{GaN} increases with P_{diss} slowly and the MC simulation temperatures are only moderately higher than the FEM results, since in this regime the heat is mainly dissipated in HS1 with a relatively large width. When the device is pinched-off and works in the saturation regime, ΔT_{GaN} increases with P_{diss} rapidly and the MC simulation-predicted temperatures are much higher than the FEM predictions, since the heat starts to be concentrated in HS2 with a much smaller size and the phonon ballistic effect is significantly enhanced.

To better reveal the bias dependence of the phonon ballistic effects, the differential thermal resistance of the GaN layer R_{diff} varying with the power dissipation P_{diss} can be computed. R_{diff} is defined as the derivative of ΔT_{GaN} versus P_{diss}, which is the slope of the curves plotted in Fig. 9. Figure 10 (a) shows the FEM-predicted R_{diff} as a function of P_{diss}. At any gate voltage, R_{diff} stays low and nearly constant with P_{diss} in the linear regime, increases rapidly when the device enters the saturation regime and reaches the same plateau value finally. This indicates that with the decrease in the heat source size, the thermal spreading effect alone can have a strong bias dependence. The MC simulation results shown in Fig. 10 (b) exhibit a similar P_{diss}-dependent behavior of R_{diff}. In both regimes, the MC simulation-predicted R_{diff} is much higher than the FEM results, and the deviations are more significant in the saturation regime due to the enhanced phonon ballistic effect with the decreased size of the heat source.

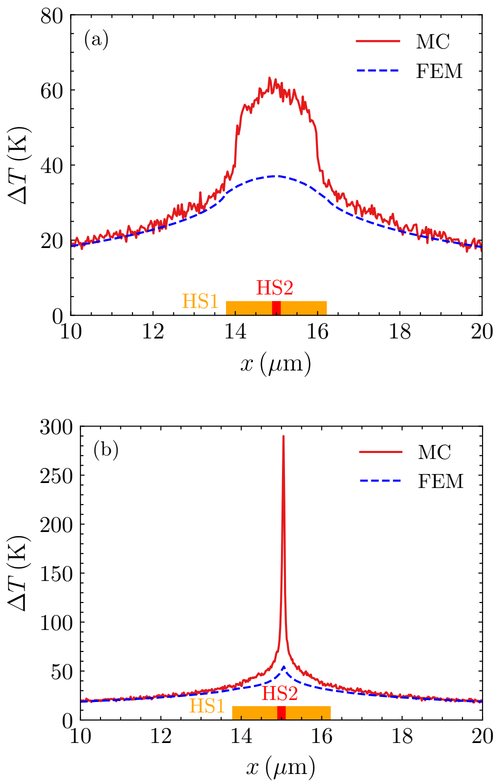

Fig. 8. Comparison of the channel temperature profiles at two biases (a) $\boldsymbol{V}_{\mathrm{g}} = 2\,\mathrm{V}, \boldsymbol{V}_{\mathrm{d}} = 3.8\,\mathrm{V}$ and (b) $\boldsymbol{V}_{\mathrm{g}} = -1\,\mathrm{V}, \boldsymbol{V}_{\mathrm{d}} = 6.7\,\mathrm{V}$ with an identical power dissipation $\boldsymbol{P}_{\mathrm{diss}} = 5\,\mathrm{W/mm}$.

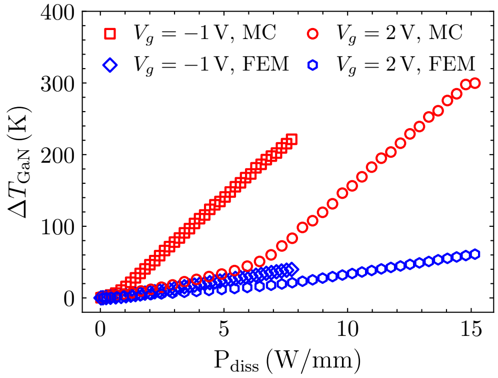

Fig. 9. Comparision of the temperature rise of the GaN layer as a function of $\boldsymbol{P}_{\mathrm{diss}}$ with between the MC simulations and FEM at different biases.

As indicated in Ref. [20], three effects can affect the thermal

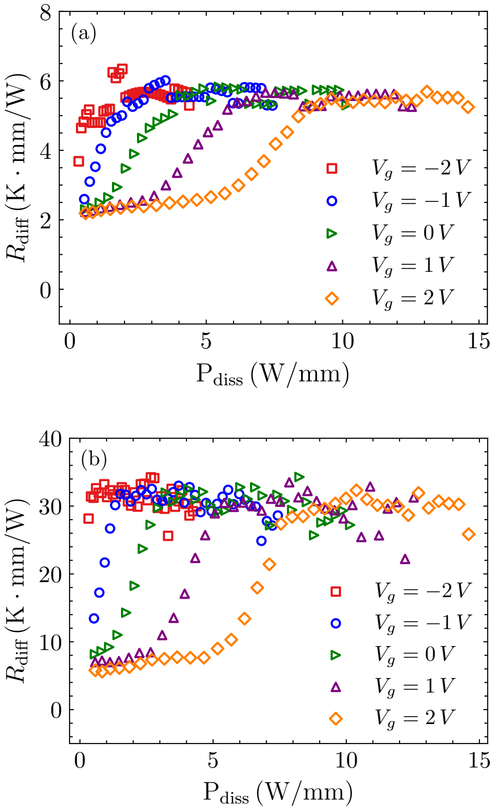

Fig. 10. Differential thermal resistance of the GaN layer $\boldsymbol{R}_{\text{diff}}$, computed as the derivative of $\boldsymbol{\Delta T}_{\text{GaN}}$ versus $\boldsymbol{P}_{\text{diss}}$ predicted by (a) FEM (b) MC simulations.

transport in the GaN layer: (1) the thermal spreading effect associated with the system shape and the size of the heat source, (2) the cross-plane ballistic effect controlled by the film thickness, and (3) the ballistic effect with the heat source size comparable with MFP. To figure out the bias dependence of the non-Fourier heat spreading process in the HEMT, the key issue here is to separate the impacts of different mechanisms. First, we focus on the influence of the cross-plane ballistic effect on thermal resistance. A dimensionless one-dimensional thermal resistance R^*_{1D} can be defined to eliminate the impacts of the thermal spreading effect and the ballistic effect with the heat source size comparable with MFP,

$$R^*_{\text{1D}} = \frac{R_{\text{1D}}}{R_{\text{1D\_0}}} \tag{3}$$

where R_{1D} is the one-dimensional thermal resistance calculated using the average temperature of the top and bottom of the GaN layer. $R_{\text{1D\_0}}$ is the one-dimension thermal resistance calculated using the bulk thermal conductivity, $R_{\text{1D\_0}} = t/(wk_0)$, where w and t are the width and thickness of the GaN layer, respectively.

As shown in Fig. 11, R^*_{1D} extracted from the MC simulations are always approximately twice the FEM results at different biases. It is because the cross-plane ballistic effect is only related to the film thickness which can be represented by using a thickness-dependent thermal conductivity of GaN films [38]. However, it should be noted that the temperatures predicted by the FEM using the thermal conductivity of GaN films are slightly lower than the MC simulation results, since the phonon-boundary scattering is enhanced with the internal heat source compared with the film in contact with two heat sinks with different temperatures [55].

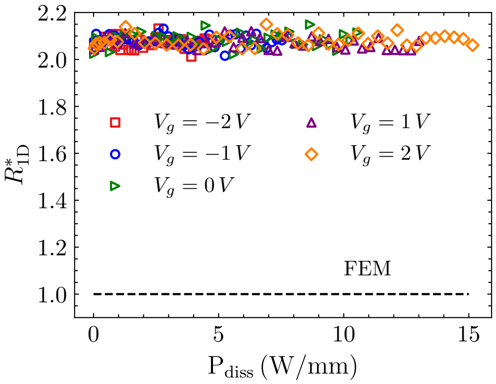

Fig. 11. Dimensionless one-dimensional thermal resistance of the GaN layer $\boldsymbol{R}^*_{\text{1D}}$ varying with $\boldsymbol{P}_{\text{diss}}$ computed by the MC simulations.

To evaluate the heat source size-induced ballistic effect, a thermal resistance ratio r_w can be defined as

$$r_w = R_{\text{diff, MC}} / \left(R_{\text{diff, FEM}} \cdot R^*_{\text{1D, MC}}\right), \tag{4}$$

where $R_{\text{diff, MC}}$ and $R_{\text{diff, FEM}}$ are the differential thermal resistance R_{diff} computed by the MC simulations and FEM, respectively. $R^*_{\text{1D, MC}}$ is the dimensionless one-dimensional thermal resistance of the GaN layer calculated by the MC simulations. The influences of the thermal spreading effect and the cross-plane ballistic effect are eliminated in $R_{\text{diff, FEM}}$ and $R^*_{\text{1D, MC}}$, respectively.

Figure 12 shows r_w varying with P_{diss} at different biases, which shows a similar pattern as Fig. 10. In the linear regime, r_w is only slightly larger than 1 and the difference between the MC simulations and FEM is dominated by the cross-plane ballistic effect. However, when the device enters the saturation regime, r_w increases rapidly and reaches a plateau value since the concentrated heat generation leads to a significant increase in the ballistic effect with heat source size comparable with MFP.

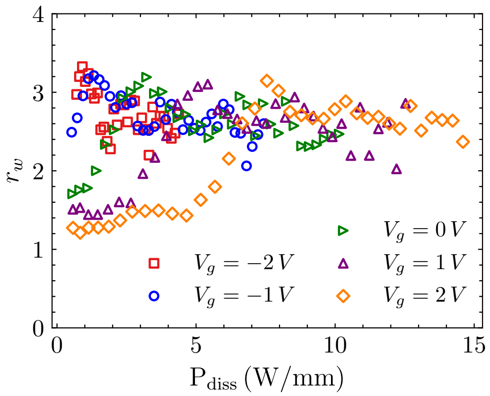

Fig. 12. Thermal resistance ratio $\boldsymbol{r_w}$ as a function of power dissipation $\boldsymbol{P}_{\text{diss}}$ at different biases.

D. Two-Thermal-Conductivity Model

Based on phonon Boltzmann transport equation (BTE) and MC simulations, the previous work has established an effective thermal conductivity model for the thermal spreading process in a ballistic-diffusive regime [20]–[22],

$$k_{\mathrm{eff}} = \frac{1}{3}\sum_j \int_0^{\omega_j} \hbar\omega \frac{\partial f_0}{\partial T}\,\mathrm{DOS}_j(\omega) v_{g,\omega,j} l_{m,j}\,\mathrm{d}\omega \tag{5}$$

Where

$$l_{m,j} = \frac{l_{0,j}}{\left(1+\frac{2}{3}Kn_{t\_\omega,j}\right)\left(1+A_w\left(\frac{w_g}{w},\frac{w}{t}\right)Kn_{w\_\omega,j}\right)r_t r_{wg}}, \tag{6}$$

in which $l_{0,j}$ is the intrinsic frequency-dependent MFP of the j branch phonon. $Kn_{t\_\omega,j} = l_{0,j}/t$ and $Kn_{w\_\omega,j} = l_{0,j}/w_g$ are the phonon branch-dependent Knudsen numbers, where t and w_g are the thickness of the GaN layer and the width of the heat generation region, respectively. In the model $1+2/3Kn_{t\_\omega,j}$ corresponds to the cross-plane ballistic effect, $1+A_w Kn_{w\_\omega,j}$ represents the ballistic effect with heat source size comparable with MFP, where A_w is a fitted parameter related to w/t and w_g/w. r_t and r_{wg} are the coefficients to reflect the influence of the phonon dispersion. When the material or the geometric parameters such as t and w_g change, the model can predict a different effective thermal conductivity to reflect the variation of the strength of the phonon ballistic effects. The model provides an easy approach to consider the influence of the ballistic effects in thermal spreading process and has been validated for different situations [21]. Using the model-predicted effective thermal conductivity, Fourier's law-based predictions can give the junction temperature close to simulation results based on phonon BTE [21]. The detailed discussions of the model can be found in Ref. [20]–[22].

In the two-heat-source model, the heat generation regions in the channel are divided into HS1 and HS2, whose widths are $L_{\mathrm{HS1}} = L_{\mathrm{finger}}$ and $L_{\mathrm{HS2}} = 0.16\,\mu\mathrm{m}$, respectively. The effective thermal conductivities corresponding to HS1 and HS2 can be easily evaluated using the effective thermal conductivity model. For the phonon properties and geometric parameters adopted in this work, k_{eff} of HS1 and HS2 are $k_{\mathrm{HS1}} = 94.47\,\mathrm{W/m\,K}$ and $k_{\mathrm{HS2}} = 47.38\,\mathrm{W/m\,K}$, respectively. The junction temperature of the GaN HEMT can then be computed by combining the two-heat-source model and the two-thermal-conductivity model,

$$T_{\mathrm{m}} = T_0 + \frac{k_{\mathrm{bulk}}}{k_{\mathrm{HS1}}}P_1R_1 + \frac{k_{\mathrm{bulk}}}{k_{\mathrm{HS2}}}P_2R_2, \tag{7}$$

where T_0 is the highest temperature at the bottom of the GaN layer calculated by the FEM, R_1 and R_2 are the thermal resistance corresponding to HS1 and HS2 of the GaN layer, respectively. It should be noted that since the heat transport in the HEMT is not a one-dimensional process, the above thermal resistance model is just an approximation to reflect the influence of the ballistic effects on the thermal resistance of the GaN HEMT.

Figure 13 shows the overall temperature rise of the HEMT at different biases calculated by the MC simulations and the model based on the FEM results, a good agreement is achieved at different biases and power dissipations. Devices with different geometries are also simulated to validate the model's applicability. Figure 14 shows the results of the devices with (a) a longer drain access region and (b) a longer gate length, which also show good consistency at different biases.

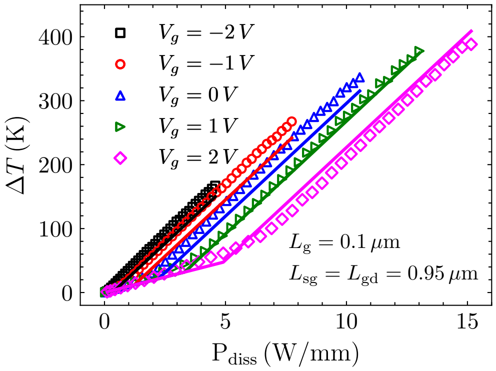

Fig. 13. Maximum temperature rise of the HEMT as a function of total power dissipation P_{diss} at different biases. The symbols are extracted from the MC simulations, and the lines are computed using the two-thermal-conductivity model based on the FEM results.

IV. CONCLUSION

In this work, non-Fourier heat spreading process in GaN HEMTs is studied by combining the TCAD and phonon MC simulations. The simulation results indicate that the bias-dependent heat generation in the channel can significantly affect the thermal spreading process and the phonon ballistic effects simultaneously. Based on the two-heat-source model, this work presents a two-thermal-conductivity model which can be easily incorporated with the FEM-based thermal analysis to reflect bias-dependent phonon ballistic transport in GaN HEMTs. The higher thermal conductivity reflects the weak ballistic effect when the channel has a relatively uniform heat distribution in the linear regime, and the lower one reflects the strong ballistic effect caused by the concentrated heat generation in the high-field region in the saturation regime. The model provides a simple approach to predict the junction temperature of the HEMT without resorting to multiscale electrothermal simulations.

REFERENCES

[1] K. Hirama, M. Kasu, and Y. Taniyasu, "Rf high-power operation of AlGaN/GaN HEMTs epitaxially grown on diamond," *IEEE electron device letters*, vol. 33, no. 4, pp. 513–515, 2012.

[2] U. K. Mishra, P. Parikh, and Y.-F. Wu, "AlGaN/GaN HEMTs-an overview of device operation and applications," *Proceedings of the IEEE*, vol. 90, no. 6, pp. 1022–1031, 2002.

[3] K. Ranjan, S. Arulkumaran, G. Ng, and A. Sandupatla, "Investigation of self-heating effect on DC and RF performances in AlGaN/GaN HEMTs on CVD-diamond," *IEEE Journal of the Electron Devices Society*, vol. 7, pp. 1264–1269, 2019.

[4] M. Rosker, C. Bozada, H. Dietrich, A. Hung, D. Via, S. Binari, E. Vivierios, E. Cohen, and J. Hodiak, "The DARPA wide band gap semiconductors for RF applications (WBGS-RF) program: Phase II results," *CS ManTech*, vol. 1, pp. 1–4, 2009.

[5] Y.-R. Wu and J. Singh, "Transient study of self-heating effects in AlGaN/GaN HFETs: Consequence of carrier velocities, temperature, and device performance," *Journal of Applied Physics*, vol. 101, no. 11, p. 113712, 2007.

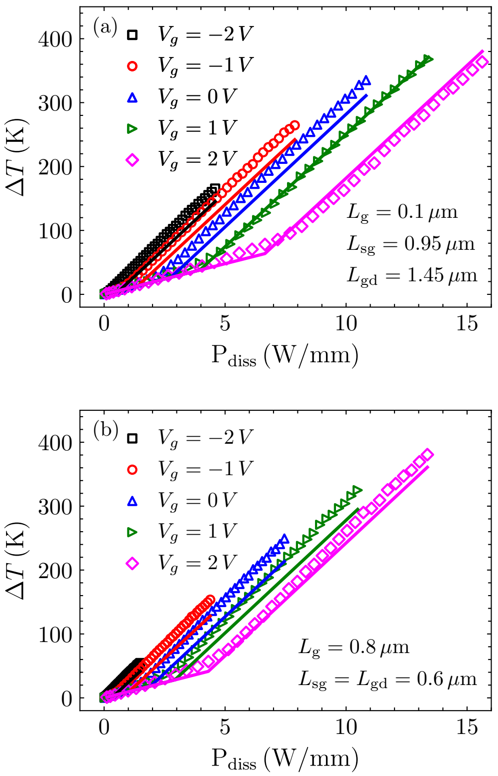

Fig. 14. Comparison of the maximum temperature rise of the HEMT versus total power dissipation P_{diss} at different biases for two more devices. (a) $L_{\text{g}} = 0.1\,\mu\text{m}, L_{\text{sg}} = 0.95\,\mu\text{m}, L_{\text{gd}} = 1.45\,\mu\text{m}$. (b) $L_{\text{g}} = 0.8\,\mu\text{m}, L_{\text{sg}} = L_{\text{gd}} = 0.6\,\mu\text{m}$. The symbols are extracted from the MC simulations, and the lines are computed using the two-thermal-conductivity model based on the FEM results.

[6] E. Heller and A. Crespo, "Electro-thermal modeling of multifinger AlGaN/GaN HEMT device operation including thermal substrate effects," *Microelectronics Reliability*, vol. 48, no. 1, pp. 45–50, 2008.

[7] J. Cho, Z. Li, M. Asheghi, and K. E. Goodson, "Near-junction thermal management: Thermal conduction in gallium nitride composite substrates," *Annual Review of Heat Transfer*, vol. 18, 2015.

[8] K. R. Bagnall, Y. S. Muzychka, and E. N. Wang, "Analytical solution for temperature rise in complex multilayer structures with discrete heat sources," *IEEE Transactions on Components, Packaging and Manufacturing Technology*, vol. 4, no. 5, pp. 817–830, 2014.

[9] M. Razavi, Y. Muzychka, and S. Kocabiyik, "Review of advances in thermal spreading resistance problems," *Journal of Thermophysics and Heat Transfer*, vol. 30, no. 4, pp. 863–879, 2016.

[10] J. P. Freedman, J. H. Leach, E. A. Preble, Z. Sitar, R. F. Davis, and J. A. Malen, "Universal phonon mean free path spectra in crystalline semiconductors at high temperature," *Scientific reports*, vol. 3, no. 1, pp. 1–6, 2013.

[11] D.-S. Tang, G.-Z. Qin, M. Hu, and B.-Y. Cao, "Thermal transport properties of GaN with biaxial strain and electron-phonon coupling," *Journal of Applied Physics*, vol. 127, no. 3, p. 035102, 2020.

[12] D. G. Cahill, P. V. Braun, G. Chen, D. R. Clarke, S. Fan, K. E. Goodson, P. Keblinski, W. P. King, G. D. Mahan, A. Majumdar *et al.*, "Nanoscale thermal transport. II. 2003–2012," *Applied physics reviews*, vol. 1, no. 1, p. 011305, 2014.

[13] Y. Hu, L. Zeng, A. J. Minnich, M. S. Dresselhaus, and G. Chen, "Spectral mapping of thermal conductivity through nanoscale ballistic transport," *Nature nanotechnology*, vol. 10, no. 8, pp. 701–706, 2015.

[14] L. Zeng, K. C. Collins, Y. Hu, M. N. Luckyanova, A. A. Maznev, S. Huberman, V. Chiloyan, J. Zhou, X. Huang, K. A. Nelson *et al.*, "Measuring phonon mean free path distributions by probing quasiballistic phonon transport in grating nanostructures," *Scientific reports*, vol. 5, no. 1, pp. 1–10, 2015.

[15] G. Chen, "Non-Fourier phonon heat conduction at the microscale and nanoscale," *Nature Reviews Physics*, vol. 3, no. 8, pp. 555–569, 2021.

[16] Y. Muzychka, J. Culham, and M. Yovanovich, "Thermal spreading resistance of eccentric heat sources on rectangular flux channels," *J. Electron. Packag.*, vol. 125, no. 2, pp. 178–185, 2003.

[17] Y. S. Muzychka, K. R. Bagnall, and E. N. Wang, "Thermal spreading resistance and heat source temperature in compound orthotropic systems with interfacial resistance," *IEEE Transactions on Components, Packaging and Manufacturing Technology*, vol. 3, no. 11, pp. 1826–1841, 2013.

[18] A. Gholami and M. Bahrami, "Thermal spreading resistance inside anisotropic plates with arbitrarily located hotspots," *Journal of Thermophysics and Heat Transfer*, vol. 28, no. 4, pp. 679–686, 2014.

[19] A. Darwish, A. J. Bayba, and H. A. Hung, "Channel temperature analysis of gan hemts with nonlinear thermal conductivity," *IEEE Transactions on Electron Devices*, vol. 62, no. 3, pp. 840–846, 2015.

[20] Y.-C. Hua, H.-L. Li, and B.-Y. Cao, "Thermal spreading resistance in ballistic-diffusive regime for GaN HEMTs," *IEEE Transactions on Electron Devices*, vol. 66, no. 8, pp. 3296–3301, 2019.

[21] Y. Shen, Y.-C. Hua, H.-L. Li, S. Sobolev, and B.-Y. Cao, "Spectral thermal spreading resistance of wide-bandgap semiconductors in ballistic-diffusive regime," *IEEE Transactions on Electron Devices*, vol. 69, no. 6, pp. 3047–3054, 2022.

[22] H.-l. Li, Y. Shen, Y.-C. Hua, S. Sobolev, and B.-Y. Cao, "Hybrid monte carlo-diffusion studies of modeling self-heating in ballistic-diffusive regime for GaN HEMTs," *Journal of Electronic Packaging*, 2022.

[23] X. Chen, S. Boumaiza, and L. Wei, "Self-heating and equivalent channel temperature in short gate length GaN HEMTs," *IEEE transactions on electron devices*, vol. 66, no. 9, pp. 3748–3755, 2019.

[24] O. Odabaşı, M. Ö. Akar, B. Bütün, and E. Özbay, "Improved t max estimation in GaN HEMTs using an equivalent hot point approximation," *IEEE Transactions on Electron Devices*, vol. 67, no. 4, pp. 1553–1559, 2020.

[25] N. Donmezer and S. Graham, "The impact of noncontinuum thermal transport on the temperature of AlGaN/GaN HFETs," *IEEE Transactions on Electron Devices*, vol. 61, no. 6, pp. 2041–2048, 2014.

[26] Q. Hao, H. Zhao, and Y. Xiao, "A hybrid simulation technique for electrothermal studies of two-dimensional GaN-on-SiC high electron mobility transistors," *Journal of Applied Physics*, vol. 121, no. 20, p. 204501, 2017.

[27] Q. Hao, H. Zhao, Y. Xiao, Q. Wang, and X. Wang, "Hybrid electrothermal simulation of a 3-d fin-shaped field-effect transistor based on GaN nanowires," *IEEE Transactions on Electron Devices*, vol. 65, no. 3, pp. 921–927, 2018.

[28] B. Chatterjee, C. Dundar, T. E. Beechem, E. Heller, D. Kendig, H. Kim, N. Donmezer, and S. Choi, "Nanoscale electro-thermal interactions in AlGaN/GaN high electron mobility transistors," *Journal of Applied Physics*, vol. 127, no. 4, p. 044502, 2020.

[29] H. Rezgui, F. Nasri, G. Nastasi, M. F. B. Aissa, S. Rahmouni, V. Romano, H. Belmabrouk, and A. A. Guizani, "Design optimization of nanoscale electrothermal transport in 10 nm SOI FinFET technology node," *Journal of Physics D: Applied Physics*, vol. 53, no. 49, p. 495103, 2020.

[30] W. Jatal, U. Baumann, K. Tonisch, F. Schwierz, and J. Pezoldt, "High-frequency performance of gan high-electron mobility transistors on 3c-sic/si substrates with au-free ohmic contacts," *IEEE Electron device letters*, vol. 36, no. 2, pp. 123–125, 2014.

[31] E. Pop, S. Sinha, and K. E. Goodson, "Heat generation and transport in nanometer-scale transistors," *Proceedings of the IEEE*, vol. 94, no. 8, pp. 1587–1601, 2006.

[32] X. Chen, S. Boumaiza, and L. Wei, "Modeling bias dependence of self-heating in GaN HEMTs using two heat sources," *IEEE Transactions on Electron Devices*, vol. 67, no. 8, pp. 3082–3087, 2020.

[33] E. Pop, "Monte carlo transport and heat generation in semiconductors," *Annual Review of Heat Transfer*, vol. 17, 2014.

[34] H. Bao, J. Chen, X. Gu, and B. Cao, "A review of simulation methods in micro/nanoscale heat conduction," *ES Energy & Environment*, vol. 1, no. 34, pp. 16–55, 2018.

[35] J.-P. M. Péraud and N. G. Hadjiconstantinou, "An alternative approach to efficient simulation of micro/nanoscale phonon transport," *Applied Physics Letters*, vol. 101, no. 15, p. 153114, 2012.

[36] H.-L. Li, J. Shiomi, and B.-Y. Cao, "Ballistic-diffusive heat conduction in thin films by phonon monte carlo method: Gray medium approximation versus phonon dispersion," *Journal of Heat Transfer*, vol. 142, no. 11, p. 112502, 2020.

[37] X. Ran and M. Wang, "A steady-state energy-based monte carlo method for phonon transport with arbitrary temperature difference," *Journal of Heat Transfer*, vol. 144, no. 8, p. 082502, 2022.

[38] C. Song, J. Kim, and J. Cho, "The effect of GaN epilayer thickness on the near-junction thermal resistance of GaN-on-diamond devices,"

International Journal of Heat and Mass Transfer, vol. 158, p. 119992, 2020.

[39] B. Danilchenko, I. Obukhov, T. Paszkiewicz, S. Wolski, and A. Jeżowski, "On the upper limit of thermal conductivity gan crystals," *Solid state communications*, vol. 144, no. 3-4, pp. 114–117, 2007.

[40] G. Chen, *Nanoscale energy transport and conversion: a parallel treatment of electrons, molecules, phonons, and photons*. Oxford university press, 2005.

[41] Q. Hao, H. Zhao, and Y. Xiao, "Multi-length scale thermal simulations of GaN-on-SiC high electron mobility transistors," in *MultiscaleThermal Transport in Energy Systems*. Nova Science Publishers, 2016.

[42] Y. Sun, Y. Zhou, M. Hu, G. Jeffrey Snyder, B. Xu, and W. Liu, "Probing the phonon mean free paths in dislocation core by molecular dynamics simulation," *Journal of Applied Physics*, vol. 129, no. 5, p. 055103, 2021.

[43] Y. Zhou, X. Gong, B. Xu, and M. Hu, "Decouple electronic and phononic transport in nanotwinned structures: a new strategy for enhancing the figure-of-merit of thermoelectrics," *Nanoscale*, vol. 9, no. 28, pp. 9987–9996, 2017.

[44] F. Alvarez, D. Jou, and A. Sellitto, "Phonon hydrodynamics and phonon-boundary scattering in nanosystems," *Journal of Applied Physics*, vol. 105, no. 1, p. 014317, 2009.

[45] R. J. Warzoha, A. A. Wilson, B. F. Donovan, N. Donmezer, A. Giri, P. E. Hopkins, S. Choi, D. Pahinkar, J. Shi, S. Graham *et al.*, "Applications and impacts of nanoscale thermal transport in electronics packaging," *Journal of Electronic Packaging*, vol. 143, no. 2, 2021.

[46] A. Manoi, J. W. Pomeroy, N. Killat, and M. Kuball, "Benchmarking of thermal boundary resistance in AlGaN/GaN HEMTs on SiC substrates: Implications of the nucleation layer microstructure," *IEEE electron device letters*, vol. 31, no. 12, pp. 1395–1397, 2010.

[47] J. Cho, E. Bozorg-Grayeli, D. H. Altman, M. Asheghi, and K. E. Goodson, "Low thermal resistances at GaN–SiC interfaces for HEMT technology," *IEEE Electron Device Letters*, vol. 33, no. 3, pp. 378–380, 2012.

[48] F. Mu, Z. Cheng, J. Shi, S. Shin, B. Xu, J. Shiomi, S. Graham, and T. Suga, "High thermal boundary conductance across bonded heterogeneous GaN–SiC interfaces," *ACS applied materials & interfaces*, vol. 11, no. 36, pp. 33 428–33 434, 2019.

[49] Y.-C. Hua and B.-Y. Cao, "A two-sensor 3ω-2ω method for thermal boundary resistance measurement," *Journal of Applied Physics*, vol. 129, no. 12, p. 125107, 2021.

[50] Y. Zhou, J.-Y. Yang, L. Cheng, and M. Hu, "Strong anharmonic phonon scattering induced giant reduction of thermal conductivity in pbte nanotwin boundary," *Physical Review B*, vol. 97, no. 8, p. 085304, 2018.

[51] Y. Hu, Y. Shen, and H. Bao, "Ultra-efficient and parameter-free computation of submicron thermal transport with phonon boltzmann transport equation," *Fundamental Research*, 2022.

[52] Y. Xu, L. Yang, and Y. Zhou, "The interfacial thermal conductance spectrum in nonequilibrium molecular dynamics simulations considering anharmonicity, asymmetry and quantum effects," *Physical Chemistry Chemical Physics*, 2022.

[53] Y. Zhou and M. Hu, "Full quantification of frequency-dependent interfacial thermal conductance contributed by two-and three-phonon scattering processes from nonequilibrium molecular dynamics simulations," *Physical Review B*, vol. 95, no. 11, p. 115313, 2017.

[54] E. Pop, R. W. Dutton, and K. E. Goodson, "Monte carlo simulation of joule heating in bulk and strained silicon," *Applied Physics Letters*, vol. 86, no. 8, p. 082101, 2005.

[55] Y.-C. Hua and B.-Y. Cao, "The effective thermal conductivity of ballistic–diffusive heat conduction in nanostructures with internal heat source," *International Journal of Heat and Mass Transfer*, vol. 92, pp. 995–1003, 2016.